Atomic structure and electronic properties of planar defects in $SrFeO_{3-\delta}$ thin films

Marta D. Rossell,[1,*] Piyush Agrawal,[1,2] Marco Campanini,[1] Daniele Passerone,[2] and Rolf Erni[1]

[1]*Electron Microscopy Center, Empa, Swiss Federal Laboratories for Materials Science and Technology, 8600 Dübendorf, Switzerland*

[2]*nanotech@surfaces laboratory, Empa, Swiss Federal Laboratories for Materials Science and Technology, 8600 Dübendorf, Switzerland*

(Received 11 May 2020; accepted 23 June 2020; published 10 July 2020)

Extended planar defects found in epitaxially grown $SrFeO_{3-\delta}$ thin films are expected to exhibit distinct conductivity properties. Here, we use a combination of scanning transmission electron microscopy techniques and electron energy-loss spectroscopy (EELS) to uncover the peculiar structure of these planar defects and to explore their electronic properties. We find that the defects are formed by $Fe_2O_{2+\alpha}$ layers consisting of FeO_5 polyhedra alternating with SrO and FeO_2 perovskite-type layers, analogous to the $Sr_4Fe_6O_{12+\delta}$ crystal structure. Our experimental and theoretical EELS data, combined with projected density of states calculations, reveal peak width changes and energies shifts, which suggest an increased electron doping of the Fe $3de_g$ band in the $Fe_2O_{2+\alpha}$ layers as compared to the $SrFeO_{3-\delta}$ film. Thus we show that the presence of $Fe_2O_{2+\alpha}$ planar defects indeed can effectively modify the electron-hole conductivity in $SrFeO_{3-\delta}$ films.

DOI: 10.1103/PhysRevMaterials.4.075001

I. INTRODUCTION

Transition metal oxides containing $3d$ metal ions in a mixed valence state are the focus of extensive research because of their rich variety of electronic, magnetic and transport phenomena. In ABX_3 perovskites (where A and B are cations and X is an anion), the most common approaches to changing the oxidation state of the B site cation use aliovalent A-site substitution [1,2] or the formation of anion vacancies [3–5]. The $SrFeO_{3-\delta}$ perovskite system belongs to the latter category exhibiting Fe ions in a mixed oxidation state ranging from 4+ (for the fully stoichiometric composition with three oxygen atoms per formula unit) to 2+ [6–9]. Actually, $SrFeO_{3-\delta}$ describes a family of five vacancy-ordered structures with the general formula $Sr_nFe_nO_{3n-1}$, where $n = \infty$, 8, 4, 2, and 1. Each phase adopts a different oxygen-vacancy arrangement in well-stablished perovskite-like structures. The $n = \infty$ end member, $SrFeO_3$, adopts the cubic perovskite structure containing FeO_6 octahedra with Fe in 4+ oxidation state. Upon reducing the oxygen content, the $n = 8$ ($Sr_8Fe_8O_{23}$) and 4 ($Sr_4Fe_4O_{11}$) members adopt tetragonal and orthorhombic structures, respectively. The oxygen vacancies in these two intermediate members form ordered arrangements accommodating iron in corner-shared oxygen FeO_6 octahedra and FeO_5 square pyramids. As a result, charge ordering of the Fe ions with different Fe^{4+} and Fe^{3+} oxidation states occurs. The $n = 2$ ($Sr_2Fe_2O_5$) member exhibits the brownmillerite-type structure which consists of alternating layers of FeO_6 octahedra and FeO_4 tetrahedra containing exclusively Fe^{3+}. Finally, the $n = 1$ ($SrFeO_2$) end member is an infinite-layer compound with FeO_4 squares and iron in Fe^{2+} state. Besides, a mixture of two neighboring oxygen vacancy-ordered phases may form for intermediate compositions with irrational n values [10,11]. But what makes this system very attractive is that it is often possible to tune from one electronic or magnetic phase to another by varying temperature, oxygen partial pressure and/or magnetic field [12–16]. Given the wide variety of possible iron oxidation states and oxygen-vacancy concentrations in the $SrFeO_{3-\delta}$ perovskite system, there is much interest in using these materials for many applications. These range from sensors, catalysts for flameless combustion, oxygen-conducting devices in solid oxide fuel cells to oxygen-conducting membranes in pressure driven oxygen generators or in partial oxidation reactors [17–20]. However, synthesizing (or tuning) a certain oxygen-deficient $SrFeO_{3-\delta}$ phase is technically very challenging and frequently results in a mixture of several phases with different oxygen deficiencies affecting bulk measurement techniques such as magnetization and resistivity [10].

Scanning transmission electron microscopy (STEM) provides the spatial resolution to investigate the structure of materials at the atomic scale. Additionally, STEM permits the simultaneous acquisition of numerous different image and spectroscopic signals while scanning the electron probe across the specimen. All these features make STEM particularly well suited to deepen our understanding of the correlation between the oxygen-vacancy ordering and the electronic properties in $SrFeO_{3-\delta}$.

In this work, we use aberration-corrected STEM in combination with energy dispersive x-ray (EDX) spectroscopy to characterize a type of ordered arrangement of oxygen vacancies forming extended planar defects in a non-stoichiometric $SrFeO_{3-\delta}$ thin film. Atomic-resolution elemental mapping by EDX is successfully employed to uncover the peculiar structure of these planar defects and to distinguish the different crystalline phases according to their chemical and structural differences. The planar defects are probed employing electron energy-loss spectroscopy (EELS) and a correlation with their electronic properties is achieved with the aid of real-space multiple-scattering simulations based on FEFF9 [21,22].

*marta.rossell@empa.ch

II. METHODS

A. Experimental details

The $SrFeO_{3-\delta}$ (SFO) thin film was deposited by pulsed laser deposition from a dense ceramic pellet consisting of pure cubic $SrFeO_3$ phase [6] using a Nd:YAG pulsed laser with tripled frequency (355 nm wavelength), 9 ns pulse length, 10 Hz repetition rate, and $3\,J/cm^2$ energy density per pulse. The film was grown epitaxially on a $SrTiO_3(001)$ substrate at an oxygen pressure of 1×10^{-2} mbar, and substrate temperature of 750 °C, as reported previously [18]. A cross-sectional sample for transmission electron microscopy was cut parallel to a cube plane of the $SrTiO_3$ substrate and mechanically polished using a tripod polisher to a thickness of about 20 μm, followed by final ion-milling under grazing incidence until electron transparency was obtained. Additionally, a cross-sectional lamella of the previously described cross-sectional sample was prepared in the orthogonal direction by means of a FEI Helios Nanolab 600i focused ion beam (FIB) instrument at accelerating voltages of 30 and 5 kV. The microstructure and the local electronic structure of the SFO film were analyzed by scanning transmission electron microscopy (STEM) using an aberration-corrected JEOL ARM200F, operated at 200 kV and equipped with a Gatan Enfinium EELS spectrometer. The STEM experiments were carried out setting a probe semi-convergence angle of 18 mrad and collecting semi-angles of 90–170 mrad for high-angle annular dark-field (HAADF) and 15–24 for annular bright-field (ABF) imaging. For the EELS data acquisition, the convergence and collection semi-angles were set to 25.3 and 33 mrad, respectively. A dispersion of 0.1 eV per channel was selected. All spectra were background subtracted by fitting a decaying power-law function to an energy window just in front of the core-loss edge onsets. Energy dispersive x-ray (EDX) spectroscopy maps were obtained using a FEI Titan Themis microscope operated at 300 kV and equipped with ChemiSTEM technology.

B. Computational details

The real-space multiple-scattering code FEFF 9.0 [22] was used for the calculation of the energy-loss near-edge structures (ELNES) of the O *K* edge as well as the projected density of states (PDOS) at different positions of the extended planar defects found in the SFO thin film. The EEL spectra were computed taking into account the same convergence and collecting semi-angles and crystallographic orientations as the experiments. A broadening of 0.4 eV was used to account for the instrumental energy resolution. The scattering potentials were calculated self-consistently over a radius of 5.93 Å using Hedin-Lundqvist (local density approximation) self-energies [23]. For the full multiple-scattering (FMS) calculations, the calculations converged for clusters as small as 154 atoms. Hence, the spectra and density-of-state calculations presented here were all modeled for 154–168 atoms in the FMS cluster. Additionally, 11 to 12 self-consistent iterations were needed to converge the total and projected density of states from FEFF calculations and we followed the procedure described in Ref. [21], which also includes an additional shift of about 2 eV in the Fermi energy to match the experimental evidence of a band gap in the material.

III. RESULTS AND DISCUSSION

A. Structural characterization

Figure 1(a) shows a low magnification HAADF-STEM micrograph of the SFO film epitaxially grown on a $SrTiO_3(001)$ substrate. The deposited film is not uniform but presents protuberances; thus, the film thickness varies between 170 and 230 nm. The out-of-plane *c* and in-plane *a* parameters were obtained from geometric phase analysis as shown in Fig. S1 of Ref. [24]. The lattice parameters obtained from

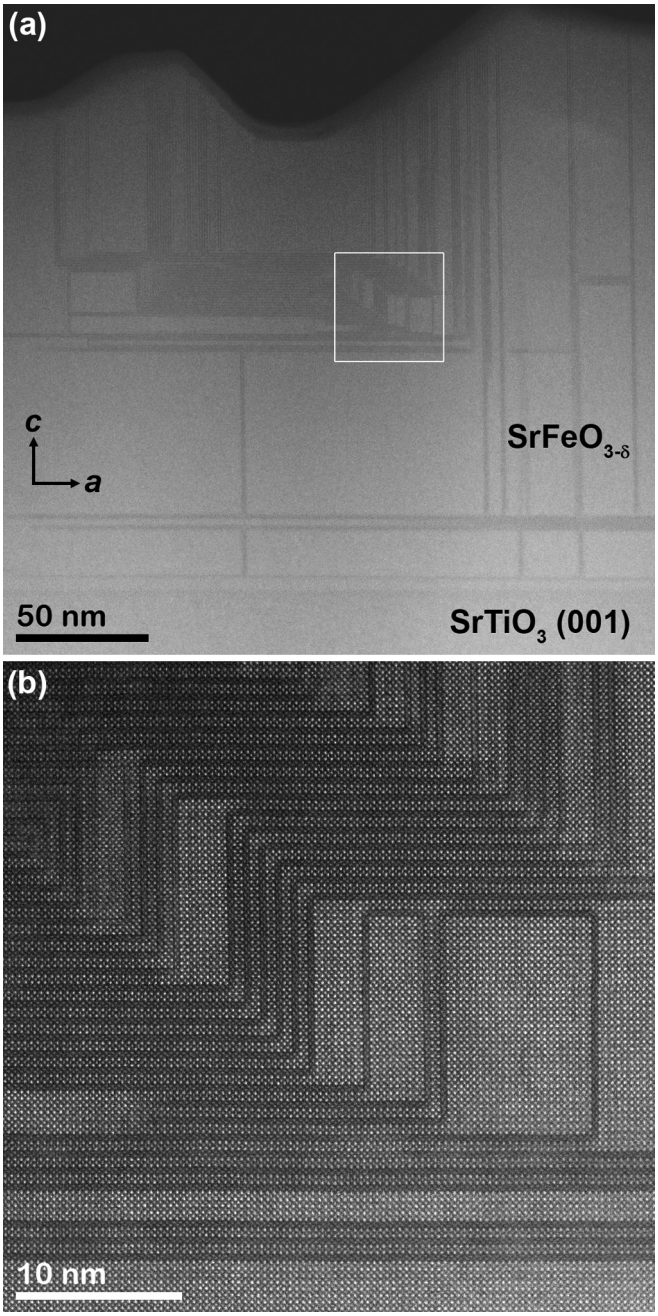

FIG. 1. (a) Low-magnification HAADF-STEM image of the SFO thin film along the [010] zone axis showing the presence of planar defects parallel and perpendicular to the growth direction. (b) Enlarged view of the square indicated in panel (a). The planar defects exhibit a darker contrast.

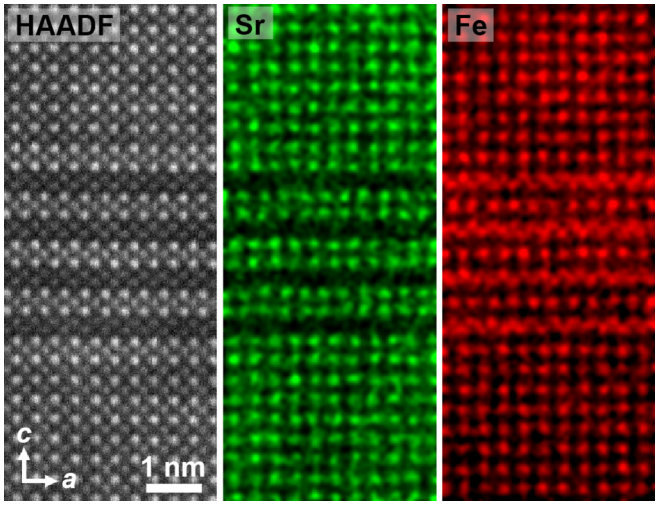

FIG. 2. HAADF-STEM survey image of four consecutive planar defects and corresponding atomic-resolution EDX elemental maps.

the strain maps using a reference lattice set in the $SrTiO_3$ substrate are 0.3878 and 0.3904 nm for the out-of-plane and in-plane parameters, respectively. Thus the measured c-axis lattice parameter is slightly larger than the value 0.3851 nm reported for cubic $SrFeO_3$ bulk samples [6], suggesting the presence of oxygen vacancies in our SFO film. Nevertheless, the exact amount of oxygen vacancies could not be estimated from the lattice parameters of the film as deviations from the Sr:Fe ratio were as well detected; see details further below.

An atomically resolved image of the area marked with a square in Fig. 1(a) is displayed in Fig. 1(b). In both images of Fig. 1, a high density of vertical (100) and horizontal (001) planar defects are clearly observable with darker contrast (see also Fig. S2 of Ref. [24]). These defects running parallel and perpendicular to the substrate surface often intersect orthogonally resulting in a labyrinth network of planar defects. Since the contrast of the atomic columns in HAADF-STEM images is approximately proportional to the mean square atomic number (Z^n with $n \approx 1.6$–1.8) of the constituent atoms, the darker planar defects are most likely to be composed of Fe.

The presence of Fe (and absence of Sr) in the planar defects was confirmed by atomic-resolution EDX mapping. Figure 2 shows a HAADF-STEM survey image of four consecutive planar defects used for EDX analysis, and the corresponding elemental atomic-resolution maps of the Sr-K and Fe-K signals extracted from the spectrum image. It is clearly visible from Fig. 2 that the planar defects consist of Fe atomic columns (red) arranged in a zigzag pattern delimited by Sr atomic columns (green). Thus these planar defects are not caused by the insertion of additional SrO rock salt-type layers in the $SrFeO_3$ structure resulting in a Ruddlesden-Popper phase as previously suggested [18]. They are also not brownmillerite structures forming in epitaxial $SrFeO_{3-\delta}$ films as the result of time- and strain-dependent structural degradation as recently observed by Wang *et al.* [25]. Instead, the planar defects investigated in this work have remained stable over more than 10 years and consist of $Fe_2O_{2+\alpha}$ layers, as explained below. Similar intergrowths were previously observed in La-doped $SrFeO_{3-\delta}$ [26].

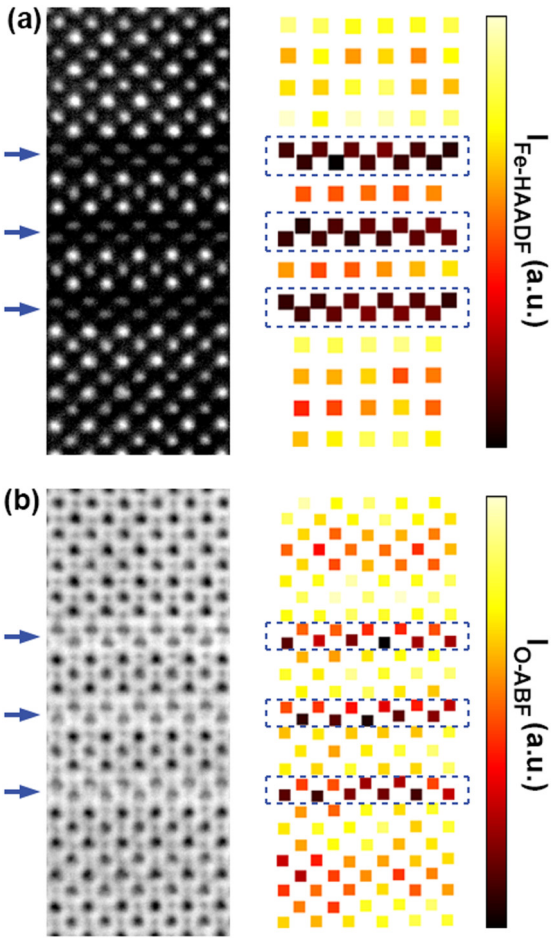

FIG. 3. (a) HAADF-STEM image of three consecutive planar defects obtained as an average of a time series consisting of 10 frames, and extracted fit of the experimental intensities for the Fe atomic columns plotted at their fitted coordinates. (b) Corresponding averaged ABF-STEM image and extracted fit of the experimental intensities for the O atomic columns plotted at their fitted coordinates. The position of the planar defects is indicated by blue arrows and dashed rectangles. Both Fe and O atomic column intensities are lower at the planar defects. The horizontal field of view is 2.3 nm.

The global chemical composition of the SFO film was also measured by EDX revealing a slight Sr deficiency, such that Sr:Fe $\approx$ 0.96:1.00 (see Fig. S3 of Ref. [24]). This slight deviation from stoichiometry might be responsible for the formation of this type of planar defects in SFO.

Simultaneously acquired HAADF- and ABF-STEM images allow visualizing the position of the lighter oxygen atoms next to the heavy Sr and Fe atomic columns (see Fig. 3). In order to improve the signal-to-noise ratio, the HAADF and ABF images of Fig. 3 were obtained as an average of a time series consisting of 10 frames, after both rigid and non-rigid registration using the Smart Align Software [27]. Due to its strong sensitivity to the atomic number, the HAADF averaged image of Fig. 3(a) was employed to map the experimental intensities of the Fe atomic columns plotted at their fitted coordinates. On the contrary, the ABF signal intensity scales approximately with $Z^{1/3}$, thus enabling the observation of the light atomic columns [28]. Making use of

ABF, we investigated the experimental intensities of the O atomic columns [Fig. 3(b)]. The fitting of the peaks in the HAADF/ABF images corresponding to the atomic columns was computed by means of seven parameters Gaussians [29]. They reveal that both Fe and O atomic columns located at the planar defects (blue dashed rectangles in Fig. 3) are arranged in a zigzag fashion and exhibit lower intensities than the rest of the structure. A plausible explanation for the observed lower intensities is that the Fe and O atoms in the planar defects are not aligned in single columns but slightly displaced in the plane perpendicular to the beam direction resulting in a different electron channeling condition that effectively reduces the image intensity of these Fe/O atomic columns. This would indeed explain that the Fe atomic columns appear elongated along the direction of the planar defects. However, we cannot rule out that the observed lower intensities are (partially) caused by the presence of Fe/O vacancies in the planar defects.

The same zigzag pattern of Fe/O atomic columns is also ascertained in the orthogonal direction, as observed in the cross-sectional FIB lamella extracted from the cross-sectional mechanically polished sample (see Fig. S4 of Ref. [24]). Thus the perovskite layers at both sides of the planar defects are shifted over $a_p/2$ (where a_p is the simple perovskite unit cell) along each orthogonal direction parallel to the planar defects. This suggests that the planar defects are indeed composed of two FeO layers together forming Fe_2O_2 double layers alternating with SrO and FeO_2 perovskite-type layers. This structure recalls the oxygen-deficient perovskite compound with the general formula $Sr_4Fe_6O_{12+\delta}$ [30–33]. A polyhedral model of the $Sr_4Fe_6O_{12+\delta}$ ($\delta = 0.74$) crystal structure [33] ($Pn2n$ space group, $a = 38.864$ Å, $b = 18.938$ Å, $c = 5.557$ Å) viewed along the [001] direction is shown in Fig. 4(a). In the $Sr_4Fe_6O_{12+\delta}$ solid solution, the FeO_6 polyhedra within the perovskite-type layers consist of corner-sharing octahedral units [shown in gray in Fig. 4(a)], while the $Fe_2O_{2+\alpha}$ double layers, with $\alpha = \delta/2$, consist of FeO_5 polyhedra arranged in bands of double edge-sharing trigonal bipyramids (in dark blue) and bands of edge-sharing tetragonal pyramids (in light blue) with variable thickness. These two types of bands are connected to each other by sharing corners. By varying the thickness of the bands consisting of tetragonal pyramids (i.e., by changing the ratio between edge- and corner-sharing FeO_5 polyhedra), different oxygen concentrations can be accommodated in the $Fe_2O_{2+\alpha}$ layers along the a direction resulting in the formation of incommensurately modulated structures. The $Sr_4Fe_6O_{12+\delta}$ crystal structure is isostructural with the large $Sr_2B_3O_{6.5-\delta}$ (B = Fe, Co, Ga) solid solution [34,35] as well as the $Ba_4In_{6-x}Mg_xO_{13-x/2}$ solid solution [36]. Therefore planar defects based on these structures are likely to form also in other perovskite-type oxides with the general formula ABO_3 with A = Sr, Ba and B = Fe, Co, Ga, In, Mg.

A model of the $Sr_4Fe_6O_{12+\delta}$ ($\delta = 0.74$) crystal structure viewed along the [107] (pseudocubic) direction is superimposed on the experimental images of Figs. 4(b) and 4(c). Additionally, calculated ADF- and ABF-STEM images for a 12-nm-thick crystal are displayed on the right side and show an excellent match with the experimental images, confirming the proposed phase model. Note here that the Fe and O atoms in the planar defects are not aligned in single columns but slightly displaced along the horizontal direction explaining the reduced image intensity and elongation of the Fe/O positions within the $Fe_2O_{2+\alpha}$ double layers. In this structure, it is likely that the differently coordinated iron ions have distinct oxidation states.

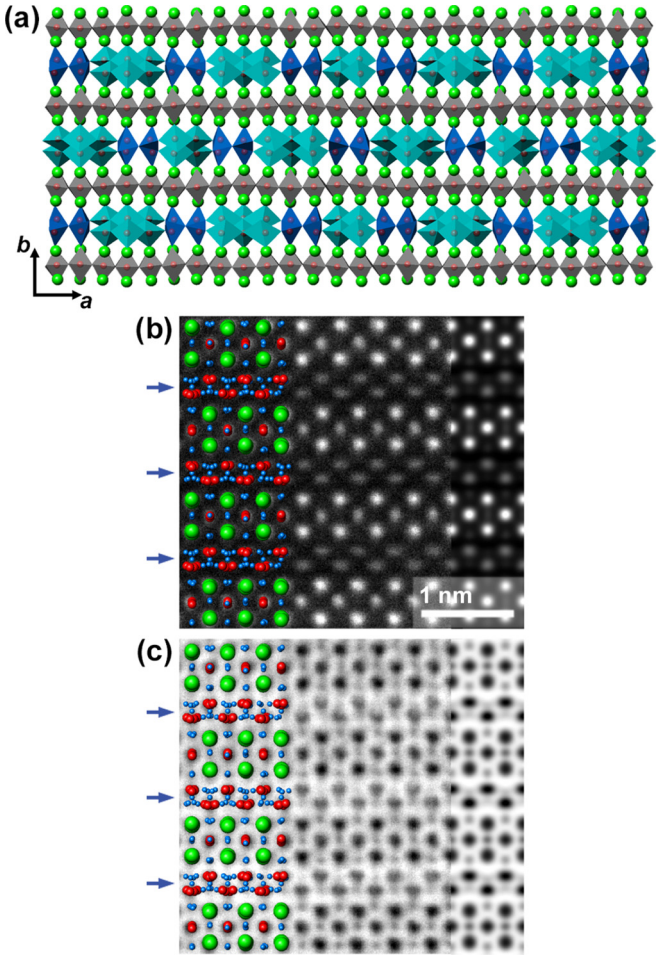

FIG. 4. (a) $Sr_4Fe_6O_{12+\delta}$ ($\delta = 0.74$) crystal structure viewed along the [001] direction. The Sr atoms are shown as green spheres and the Fe atoms are located in the shaded polyhedra. $Fe_2O_{2+\alpha}$ double layers of FeO_5 polyhedra (in blue) alternate along the b-direction with perovskite-type layers of FeO_6 octahedra (in gray). (b) Experimental HAADF-STEM image with overlaid calculated image for a 12-nm-thick crystal (right). (c) Experimental ABF-STEM image with overlaid calculated image for a 12-nm-thick crystal (right). The structural models superimposed on the experimental images are viewed along [107]. The Sr, Fe, and O atoms are shown in green, red, and blue, respectively. Blue arrows indicate the position of the planar defects ($Fe_2O_{2+\alpha}$ double layers).

B. EEL spectroscopy studies

EELS is used to investigate the oxidation state of the iron ions in the non-stoichiometric $SrFeO_{3-\delta}$ thin film by probing the Fe $L_{2,3}$ and the O K edges. The EELS fine structure (namely the energy-loss near-edge structure ELNES) of a core-loss edge has been proven useful to provide information about the oxidation state and the local coordination of the

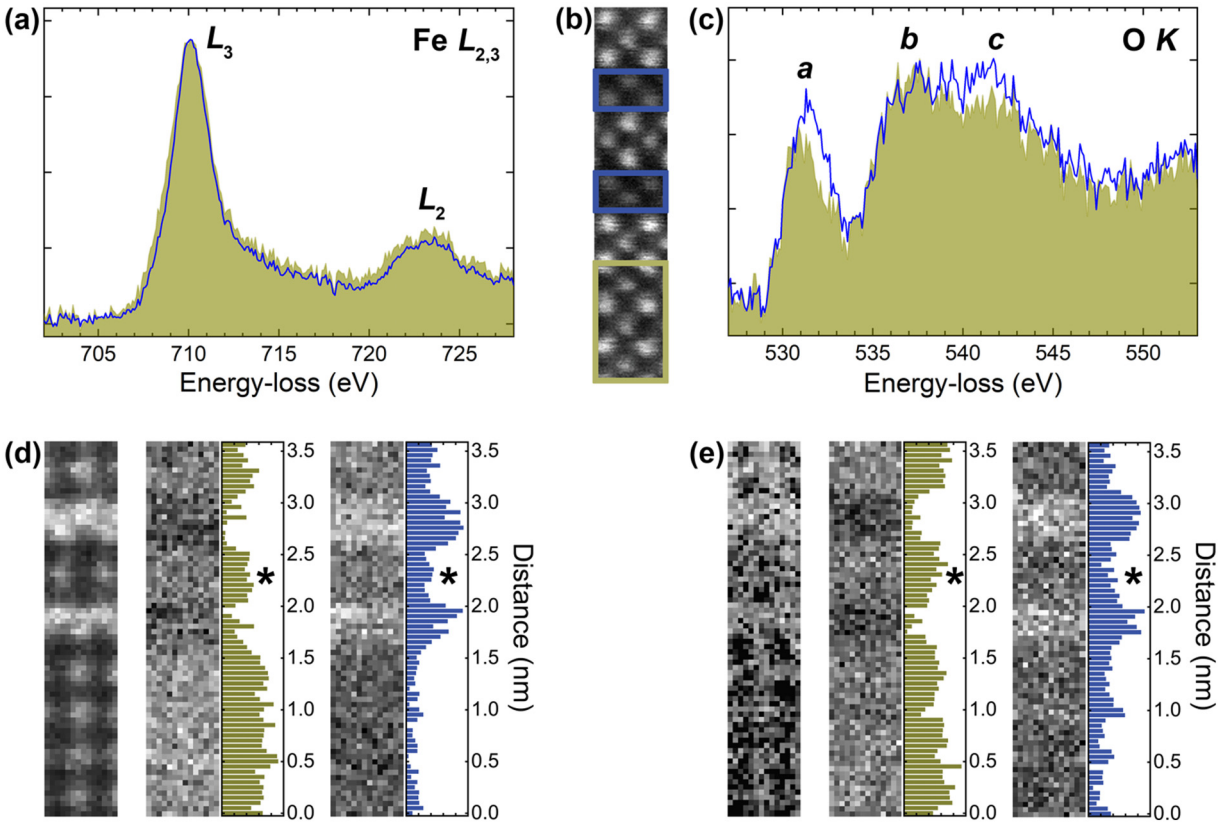

FIG. 5. EELS data of two planar defects acquired at atomic spatial resolution. (a) Fe $L_{2,3}$ edge summed over three octahedral layers (kaki) and two planar defects (blue). (b) Survey image indicating with rectangles the areas used for Fe^{4+} (kaki) and reduced Fe (blue) summation. The horizontal field of view is 0.7 nm. (c) O *K* edge summed over three octahedral layers (kaki) and two planar defects (blue). (d) Atomic-resolution map of the Fe $L_{2,3}$ edge, and corresponding Fe^{4+} and reduced Fe maps generated by fitting the averaged components to the atomic resolution data. (e) Atomic-resolution map of the O *K* edge, and corresponding EELS maps generated by fitting the average components to the atomic resolution data. The intensity profiles of all components are extracted over the full image widths.

atom undergoing excitation. Thus, using a combination of HAADF-STEM and EELS in an aberration-corrected microscope, 2D atomic mapping of cation valence states in mixed valence compounds was demonstrated [37,38]. Likewise, site-specific mapping of the oxygen coordination number for transition metals in mixed coordination/single-valency compounds was also reported [39,40]. The analysis becomes more complicated when the change in bonding coincides with a change in oxidation state affecting also the EELS fine structure, as in the case of the mixed-valence oxygen deficient $SrFeO_{3-\delta}$ system [6,7,41–44]. However, in general, changes in the fine structure of the $L_{2,3}$ edge of the transition metals due to bonding or coordination are more subtle than changes related to the oxidation state.

An atomically resolved EELS spectrum image acquired across two planar defects is shown in Fig. 5. Figure 5(b) is the overview HAADF-STEM image of the analyzed area showing the presence of two planar defects (blue rectangles) surrounded by perovskite-type blocks. Figures 5(a) and 5(c) are the Fe $L_{2,3}$ and O *K* edges, respectively, after background subtraction and averaged over the areas marked with blue and kaki rectangles in the survey image of Fig. 5(b). Thus the kaki (filled) spectra are summed over the three bottom perovskite-type layers and the blue (empty) spectra are averaged over the two planar defects. Clear differences in the Fe $L_{2,3}$ and O *K* fine structures can be identified by simple visual inspection.

The Fe $L_{2,3}$ edge corresponds to excitations of the Fe $2p$ electrons into empty Fe $3d$ states. The spectra in Fig. 5(a) are characterized by the occurrence of two main features, known as white lines. They are separated by 13.1 eV due to spin-orbit splitting of the Fe $2p$ core hole into $2p_{3/2}$ and $2p_{1/2}$ states, labeled as L_3 and L_2, respectively. To facilitate the visual comparison of the data, both spectra were normalized to the L_3 edge. Significantly different L_3/L_2 white-line intensity ratios and L_3 line widths are observed for each phase suggesting that the oxidation state of Fe is not equivalent. The broader L_3 peak without shoulder structures corresponding to the perovskite-type blocks is very similar to that of $SrFeO_3$ previously measured by x-ray absorption spectroscopy [1] and EELS [45]. This broad peak reflects the strong hybridization in $SrFeO_3$ and is quite similar to the one observed in $BaFeO_3$ [46] suggesting that the valence of Fe is equal (or close) to 4+. On the other hand, the narrower L_3 line measured at the planar defects indicates a decrease of the nominal oxidation state of iron to Fe^{3+} and Fe^{2+} (see explanation further below).

Complementary information is obtained from the O *K* edge, resulting from excitations of O $1s$ electrons into available O $2p$ empty states. Figure 5(c) shows the O *K* near-edge

structure of both the $Fe_2O_{2+\alpha}$ double layers and the SFO perovskite-type phase unveiling three major peaks, *a*, *b*, and *c*, caused by hybridizations of unoccupied O 2*p* orbitals with Fe 3*d*, Sr 4*d*, and Fe 4*sp* orbitals, respectively [1,47]. For clarity, the spectra were normalized to the intensity maxima of the main peak *b*. According to earlier reports, since the O K_a pre-peak has a very strong contribution from the Fe $3de_g$ band occupancy, it can be used to extract information on the Fe oxidation state [2,48]. Thus the energy difference between the oxygen O K_b main peak and the O K_a pre-peak can be used to estimate the local oxidation state in the two phases. This energy difference is about 5.9 eV for the planar defects and 6.3 eV for the perovskite-type blocks. The smaller energy difference exhibited by the planar defect (blue) spectrum suggests an increased electron doping of the Fe $3de_g$ band, that is to the transition $Fe^{4+} \rightarrow Fe^{3+}/Fe^{2+}$, in good agreement with the Fe $L_{2,3}$ edge observations and with previous reports [1,47].

The above described ELNES of both the Fe $L_{2,3}$ and O *K* edges are in excellent agreement with the ones previously reported for $Sr_4Fe_6O_{12.74}$ [33]. Next, we used the differences in the fine structure of the Fe $L_{2,3}$ edge to map the Fe oxidation state in the film using the averaged EELS signals from Fig. 5(a) as internal references. The internal reference data for Fe in the two distinct oxidation states are fitted to the entire acquired EELS data cube in a linear combination by applying the multiple linear least-squares (MLLS) fitting routine of Digital Micrograph™ [49]. This allows generating 2D component maps of the spectral weights. The results of the fit are displayed in Fig. 5(d). For clarity, intensity profiles of the two components (namely oxidized Fe^{4+} and reduced Fe) are extracted over the full image widths. It is clear that iron is in a reduced state at the planar defects, and in higher oxidation state (i.e., close to Fe^{4+}) at the SFO perovskite-type layers located at the bottom of the spectrum image. However, the perovskite-type layer (marked with an asterisk) placed between the two $Fe_2O_{2+\alpha}$ double layers exhibits an oxidation state, which falls in between the $Fe_2O_{2+\alpha}$ double layers and the SFO phase at the bottom. Considering that the average oxidation state of the $Sr_4Fe_6O_{12.74}$ crystal structure is $Fe^{2.9+}$, it is safe to assume that charge ordering of the Fe ions occurs in the alternating layers, such that the FeO_6 octahedra in the perovskite-type layers contain exclusively Fe^{3+}, while the FeO_5 polyhedra in the double layers contain iron in Fe^{3+} and Fe^{2+} oxidation states. Hence, the differently coordinated iron ions have distinct oxidation states.

Likewise, the summed O *K* ELNES signatures from Fig. 5(c) were used to generate 2D component maps of the spectral weights. The results of the fit are displayed in Fig. 5(e) and show a trend comparable to the one discussed for the Fe $L_{2,3}$ edge.

C. Interpretation of the EEL spectra

We have compared our experimental spectra with theoretical ELNES to interpret the spectral features appearing in the oxygen *K* edge spectra obtained at the $Fe_2O_{2+\alpha}$ double and the FeO_2 perovskite-type layers. For this purpose, we used the model based on the $Sr_4Fe_6O_{12+\alpha}$ ($\delta = 0.74$) crystal structure [33] [see Fig. 4(a)]. For full details on the multiple-scattering calculations of the O *K* ELNES and the PDOS, we refer the reader to Sec. II B. Computational details.

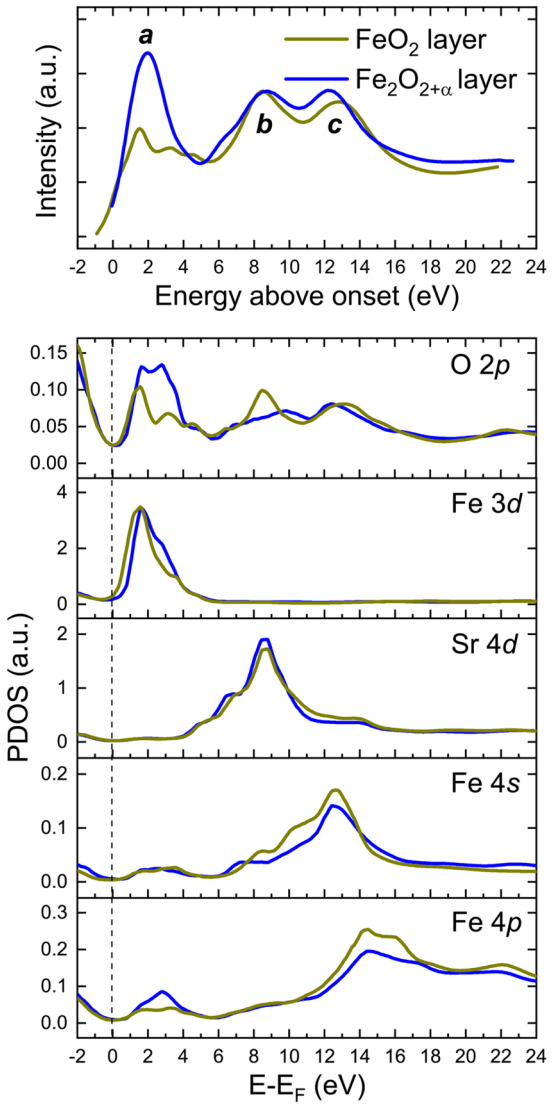

FIG. 6. Oxygen *K* energy-loss near-edge structures and projected density of states (PDOS) calculated for the (blue) $Fe_2O_{2+\alpha}$ double and (kaki) FeO_2 perovskite-type layers. Contributions from the different atomic orbitals for the O, Fe, and Sr atomic species are given in separate panels.

The calculated O *K* edge spectra of both $Fe_2O_{2+\alpha}$ and FeO_2 layers are shown in Fig. 6. They reflect the integral of several nonequivalent oxygen environments in each layer. Similarly to our experimental data, the calculated spectra show three major peaks, *a*, *b*, and *c*. Here again, for clarity, the spectra were normalized to the intensity maxima of the *b* peak. It can be seen that the calculations succeed to predict correctly the relative position and intensity of all peaks, except for the *a* peak intensity of the $Fe_2O_{2+\alpha}$ layer spectrum. This discrepancy with the experiments is attributed to the theoretical calculations not including multiplet effects, which are important when calculating excitations involving 3*d* electrons. Nevertheless, in overall, the calculations correctly predict the differences in the electronic structure observed experimentally.

Shown in Fig. 6 is as well the projected density of states (PDOS) of the O $2p$, Fe $3d$, Sr $4d$, Fe $4s$, and Fe $4p$ states in the $Fe_2O_{2+\alpha}$ (blue) and FeO_2 (kaki) layers. Similar to previous studies [1,47], we found that the *a* peak mostly stems from transitions to hybridized O $2p$-Fe $3d$ orbitals (although some Fe $4sp$ states are located in this range, too), while the post-edge region of the spectra is caused by hybridizations of unoccupied O $2p$ orbitals with Sr $4d$ (peak *b*) and Fe $4sp$ (peak *c*) orbitals. However, when comparing the PDOS of the $Fe_2O_{2+\alpha}$ and FeO_2 layers, it is evident that the O $2p$ and Fe $3d$ peaks at ∼2 eV markedly vary in the two layers. The O $2p$ and Fe $3d$ peaks are shifted to higher energies for the $Fe_2O_{2+\alpha}$ layer. In addition, a splitting of the O $2p$ peak in this layer is evident, revealing the diverse site coordination of the Fe atoms in the $Fe_2O_{2+\alpha}$ double layer (namely trigonal bipyramids and tetragonal pyramids), which is determined by the nearest oxygen neighbors. This results in a broadening and a shift of the O K_a EELS peak of the $Fe_2O_{2+\alpha}$ layer to higher energies, suggesting a reduced oxidation state and an increased electron doping of the Fe $3de_g$ band in the double layers as compared to the $SrFeO_{3-\delta}$ film. This is in good agreement with previously reported electron-hole conductivity measurements in epitaxial $Sr_4Fe_6O_{12+\delta}$ films, which showed that the conductivity of the films is considerably affected by the oxygen content in the oxygen deficient $Fe_2O_{2+\alpha}$ double layers [50–53].

IV. CONCLUSIONS

In conclusion, aberration-corrected STEM has been used to assess the atomic structure of extended planar defects present in epitaxially grown $SrFeO_{3-\delta}$ thin films. HAADF-, ABF-STEM, and elemental EDX mapping have been employed to identify the chemical nature of the planar defects. They consist of $Fe_2O_{2+\alpha}$ double layers of FeO_5 polyhedra alternating with SrO and FeO_2 perovskite-type layers in an ordered arrangement that resembles the $Sr_4Fe_6O_{12+\delta}$ crystal structure. The $Sr_4Fe_6O_{12+\delta}$ intergrowths intersect orthogonally resulting in an extraordinary labyrinth network of planar defects in the $SrFeO_{3-\delta}$ thin films. Their effect on the electronic properties has been investigated by EELS and interpreted with the aid of simulations based on the real-space multiple-scattering code FEFF9. Our experimental and theoretical data reveal peak-width changes and energies shifts, which suggest an increased electron doping of the Fe $3de_g$ band in the $Fe_2O_{2+\alpha}$ layers as compared to the $SrFeO_{3-\delta}$ film. These results clarify the exact atomic structure of the planar defects in $SrFeO_{3-\delta}$ and suggest that their presence might substantially alter the electron-hole conductivity in the $SrFeO_{3-\delta}$ films.

ACKNOWLEDGMENTS

The authors are thankful to C. Solís and J. Santiso for the samples used in this study. This research was supported by the Swiss National Science Foundation (SNSF) under project Nos. 200021_147105 and 200021_175926. Access to the TEM facilities at IBM Research-Zurich, Switzerland, under the IBM/Empa Master Joint Development Agreement is gratefully acknowledged.

[1] M. Abbate, F. M. F. de Groot, J. C. Fuggle, A. Fujimori, O. Strebel, F. Lopez, M. Domke, G. Kaindl, G. A. Sawatzky, M. Takano, Y. Takeda, H. Eisaki, and S. Uchida, Phys. Rev. B **46**, 4511 (1992).

[2] M. Varela, M. P. Oxley, W. Luo, J. Tao, M. Watanabe, A. R. Lupini, S. T. Pantelides, and S. J. Pennycook, Phys. Rev. B **79**, 085117 (2009).

[3] T. Moriga, O. Usaka, T. Imamura, I. Nakabayashi, I. Matsubara, T. Kinouchi, S. Kikkawa, and F. Kanamaru, Bull. Chem. Soc. Jpn. **9**, 687 (1994).

[4] T. C. Gibb, A. J. Herod, D. C. Munro, and N. Peng, J. Mater. Chem. **5**, 1909 (1995).

[5] R. Le Toquin, W. Paulus, A. Cousson, C. Prestipino, and C. Lamberti, J. Am. Chem. Soc. **128**, 13161 (2006).

[6] J. P. Hodges, S. Short, J. D. Jorgensen, X. Xiong, B. Dabrowski, S. M. Mini, and C. W. Kimball, J. Solid State Chem. **151**, 190 (2000).

[7] M. Schmidt, M. Hofmann, and S. J. Campbell, J. Phys.: Condens. Matter **15**, 8691 (2003).

[8] Y. Tsujimoto, C. Tassel, N. Hayashi, T. Watanabe, H. Kageyama, K. Yoshimura, M. Takano, M. Ceretti, C. Ritter, and W. Paulus, Nature **450**, 1062 (2007).

[9] L. Wang, Z. Yang, M. E. Bowden, and Y. Du, Appl. Phys. Lett. **114**, 231602 (2019).

[10] S. H. Lee, T. W. Frawley, C. H. Yao, Y. C. Lai, C.-H. Du, P. D. Hatton, M. J. Wang, F. C. Chou, and D. J. Huang, New. J. Phys. **18**, 093033 (2016).

[11] B. C. Tofield, G. Greaves, and B. E. F. Fender, Mat. Res. Bull. **10**, 737 (1975).

[12] Y. M. Zhao, R. Mahendiran, N. Nguyen, B. Raveau, and R. H. Yao, Phys. Rev. B **64**, 024414 (2001).

[13] M. Schmidt and S. J. Campbell, J. Phys. Chem. Solids **63**, 2085 (2002).

[14] A. Lebon, P. Adler, C. Bernhard, A.V. Boris, A. V. Pimenov, A. Maljuk, C. T. Lin, C. Ulrich, and B. Keimer, Phys. Rev. Lett. **92**, 037202 (2004).

[15] P. Adler, A. Lebon, V. Damljanović, C. Ulrich, C. Bernhard, A. V. Boris, A. Maljuk, C. T. Lin, and B. Keimer, Phys. Rev. B **73**, 094451 (2006).

[16] S. Ishiwata, M. Tokunaga, Y. Kaneko, D. Okuyama, Y. Tokunaga, S. Wakimoto, K. Kakurai, T. Arima, Y. Taguchi, and Y. Tokura, Phys. Rev. B **84**, 054427 (2011).

[17] J. B. MacChesney, R. C. Sherwood, and J. F. Potter, J. Chem. Phys. **43**, 1907 (1965).

[18] C. Solís, M. D. Rossell, G. Garcia, A. Figueras, G. Van Tendeloo, and J. Santiso, Solid State Ionics **179**, 1996 (2008).

[19] H. Falcón, J. A. Barbero, J. A. Alonso, M. J. Martínez-Lop, and J. L. G. Fierro, Chem. Mater. **14**, 2325 (2002).

[20] B. C. H. Steele, Curr. Opin. Solid State Mater. Sci. **1**, 684 (1996).

[21] M. S. Moreno, K. Jorissen, and J. J. Rehr, Micron **38**, 1 (2007).

[22] J. J. Rehr, J. J. Kas, F. D. Vila, M. P. Prange, and K. Jorissen, Phys. Chem. Chem. Phys. **12**, 5503 (2010).

[23] L. Hedin and S. Lundqvist, Solid State Phys. **23**, 1 (1970).

[24] See Supplemental Material at http://link.aps.org/supplemental/10.1103/PhysRevMaterials.4.075001 for the geometrical phase analysis (GPA) and energy dispersive x-ray (EDX) spectroscopy analysis of the $SrFeO_{3-\delta}$ film, and additional HAADF-STEM images of the planar defects.

[25] L. Wang, Z. Yang, J. Wu, M. E. Bowden, W. Yang, A. Qiao, and Y. Du, NPJ Mater. Degrad. **4**, 16 (2020).

[26] R. Bredesen, T. Norby, A. Bardal, and V. Lynum, Solid State Ionics **135**, 687 (2000).

[27] L. Jones, H. Yang, T. J. Pennycook, M. S. J. Marshall, S. Van Aert, N. D. Browning, M. R. Castell, and P. D. Nellist, Adv. Struct. & Chem. Imaging **1**, 8 (2015).

[28] S.D. Findlay, N. Shibata, H. Sawada, E. Okunishi, Y. Kondo, and Y. Ikuhara, Ultramicroscopy **110**, 903 (2010).

[29] A. B. Yankovich, B. Berkels, W. Dahmen, P. Binev, S. I. Sanchez, S. A. Bradley, A. Li, I. Szlufarska, and P. M. Voyles, Nat. Comm. **5**, 4155 (2014).

[30] M. D. Rossell, A. M. Abakumov, G. Van Tendeloo, J. A. Pardo, and J. Santiso, Chem. Mater. **16**, 2578 (2004).

[31] M. D. Rossell, A. M. Abakumov, G. Van Tendeloo, M. V. Lomakov, S. Ya. Istomin, and E. V. Antipov, Chem. Mater. **17**, 4717 (2005).

[32] B. Mellenne, R. Retoux, C. Lepoittevin, M. Hervieu, and B. Raveau, Chem. Mater. **16**, 5006 (2004).

[33] M. D. Rossell, A. M. Abakumov, Q. M. Ramasse, and R. Erni, ACS Nano **7**, 3078 (2013).

[34] D. Pelloquin, S. Hébert, O. Perez, V. Pralong, N. Nguyen, and A. Maignan, J. Solid State Chem. **178**, 792 (2005).

[35] H. Desmoulins, S. Malo, O. Perez, D. Pelloquin, A. Maignan, and M. Hervieu, Chem. Mater. **23**, 2786 (2011).

[36] A. M. Abakumov, M. D. Rossell, O. Yu. Gutnikova, O. A. Drozhzhin, L. S. Leonova, Y. A. Dobrovolsky, S. Ya. Istomin, G. Van Tendeloo, and E. V. Antipov, Chem. Mater. **20**, 4457 (2008).

[37] H. Tan, S. Turner, E. Yücelen, J. Verbeeck, and G. Van Tendeloo, Phys. Rev. Lett. **107**, 107602 (2011).

[38] S. Turner, S. Lazar, B. Freitag, R. Egoavil, J. Verbeeck, S. Put, Y. Strauven, and G. Van Tendeloo, Nanoscale **3**, 3385 (2011).

[39] S. Turner, J. Verbeeck, F. Ramezanipour, J. E. Greedan, G. Van Tendeloo, and G. A. Botton, Chem. Mater. **24**, 1904 (2012).

[40] S. Turner, R. Egoavil, M. Batuk, A. A. Abakumov, J. Hadermann, J. Verbeeck, and G. Van Tendeloo, Appl. Phys. Lett. **101**, 241910 (2012).

[41] R. Vidya, P. Ravindran, H. Fjellvåg, and A. Kjekshus, Phys. Rev. B **74**, 054422 (2006).

[42] P. Adler, Phys. Rev. B **77**, 136401 (2008).

[43] P. Ravindran, R. Vidya, H. Fjellvåg, and A. Kjekshus, Phys. Rev. B **77**, 134448 (2008).

[44] P. Ravindran, R. Vidya, H. Fjellvåg, and A. Kjekshus, Phys. Rev. B **77**, 136402 (2008).

[45] A. Feldhoff, J. Martynczuk, M. Arnold, M. Myndyk, I. Bergmann, V. Šepelák, W. Gruner, U. Vogt, A. Hähnel, and J. Woltersdorf, J. Solid State Chem. **182**, 2961 (2009).

[46] T. Tsuyama, T. Matsuda, S. Chakraverty, J. Okamoto, E. Ikenaga, A. Tanaka, T. Mizokawa, H. Y. Hwang, Y. Tokura, and H. Wadati, Phys. Rev. B **91**, 115101 (2015).

[47] V. R. Galakhov, E. Z. Kurmaev, K. Kuepper, M. Neumann, J. A. McLeod, A. Moewes, I. A. Leonidov, and V. L. Kozhevnikov, J. Phys. Chem. C **114**, 5154 (2010).

[48] P. Agrawal, J. Guo, P. Yu, C. Hébert, D. Passerone, R. Erni, and M. D. Rossell, Phys. Rev. B **94**, 104101 (2016).

[49] GATAN Microscopy Suite Software is available from www.gatan.com/products/tem-analysis/gatan-microscopy-suite-software.

[50] B. Ma and U. Balachandran, Solid State Ionics **100**, 53 (1997).

[51] S. Guggilla and A. Manthiram, J. Electrochem. Soc. **144**, L120 (1997).

[52] J. C.Waerenborgh, M. Avdeev, M. V. Patrakeev, V. V. Kharton, and J. R. Frade, Mater. Lett. **57**, 3245 (2003).

[53] C. Solís, W. Jung, H. L. Tuller, and J. Santiso, Chem. Mater. **22**, 1452 (2010).